

1 **Dynamic rupture process of the 2023  $M_w$  7.8 Kahramanmaraş earthquake (SE**  
2 **Türkiye): Variable rupture speed and implications for seismic hazard**

3 **Zijia Wang<sup>1</sup>, Wenqiang Zhang<sup>2</sup>, Tuncay Taymaz<sup>3</sup>, Zhongqiu He<sup>1</sup>, Tianhong Xu<sup>1</sup>,**  
4 **Zhenguo Zhang<sup>1,4</sup>**

5 <sup>1</sup>Department of Earth and Space Sciences, Southern University of Science and Technology,  
6 Shenzhen, China.

7 <sup>2</sup>Department of Earth and Planetary Sciences, McGill University, Montreal, Canada

8 <sup>3</sup>Department of Geophysical Engineering, The Faculty of Mines, Istanbul Technical  
9 University, Maslak, Sarıyer, Istanbul, Türkiye

10 <sup>4</sup>Guangdong Provincial Key Laboratory of Geophysical High-resolution Imaging Technology,  
11 Southern University of Science and Technology, Shenzhen, China

12 Corresponding author: Zhenguo Zhang ([zhangzg@sustech.edu.cn](mailto:zhangzg@sustech.edu.cn))

13  
14 **Key Points:**

- 15 • The high initial stress accumulated in the seismic gap leads to the successful  
16 triggering of the East Anatolian Fault.
- 17 • The change of fault geometry in the southwest segment prevented the sustained  
18 supershear rupture.
- 19 • The risk of earthquake nucleation on the secondary fault triggering the major fault  
20 rupture and the related disaster was highlighted.

22 **Abstract**

23 We considered various non-uniformities such as branch faults, rotation of stress field  
24 directions, and changes in tectonic environments to simulate the dynamic rupture process of  
25 the 6<sup>th</sup> February 2023  $M_w$  7.8 Kahramanmaraş earthquake in SE Türkiye. We utilized near-  
26 fault waveform data, GNSS static displacements, and surface rupture to constrain the  
27 dynamic model. The results indicate that the high initial stress accumulated in the  
28 Kahramanmaraş-Çelikhan seismic gap leads to the successful triggering of the East Anatolian  
29 Fault (EAF) and the supershear rupture in the northeast segment. Due to the complexity of  
30 fault geometry, the rupture speed along the southeastern segment of the EAF varied  
31 repeatedly between supershear and subshear, which contributed to the unexpectedly strong  
32 ground motion. Furthermore, the triggering of the EAF reminds us to be aware of the risk of  
33 seismic gaps on major faults being triggered by secondary faults, which is crucial to prevent  
34 significant disasters.

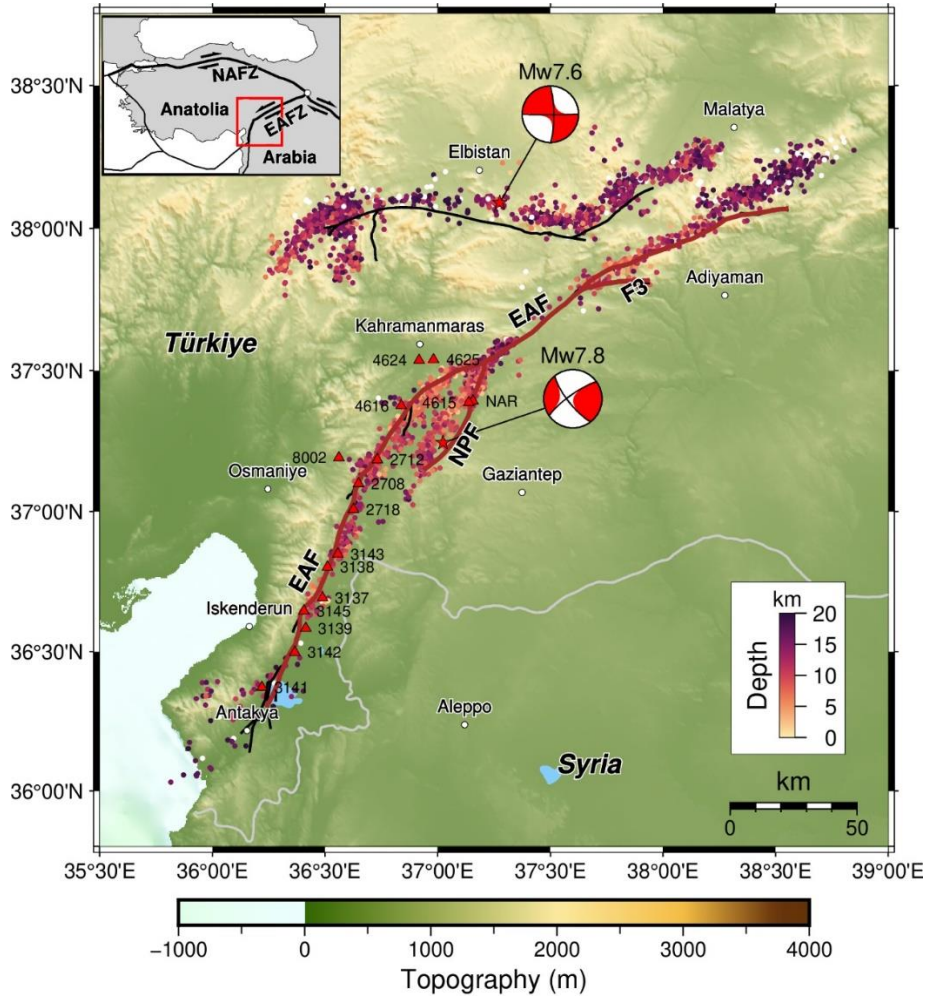
35 **Plain Language Summary**

36 On February 6, 2023, the south-central Türkiye was hit by two major earthquakes with  
37 magnitudes of  $M_w$  7.8 and  $M_w$  7.6 respectively. Among them, the complex rupture process  
38 and unexpected ground motion of the  $M_w$  7.8 event attracted the attention of seismologists. In  
39 this paper, the 3D dynamic rupture process of this mainshock is simulated based on complex  
40 multi-fault system and heterogeneous initial stress. And the simulation results are in good  
41 agreement with the observations. Our results show that high initial stress is required for the  
42 EAF to be triggered. The supershear rupture occurred only in certain fault segments and is  
43 unable to sustain itself in a significant area on the fault due to the along-strike variations in

44 fault geometry and strength. More importantly, the dynamic model suggests that we must be  
45 alert to the risk of major fault being triggered by earthquakes on nearby small faults,  
46 especially when there are seismic gaps on the major fault.

## 47 **1 Introduction**

48 On 6<sup>th</sup> February 2023, at 01:17:34 UTC, the  $M_w$  7.8 earthquake struck the Nurdağı-Pazarcık  
49 region in the Kahramanmaraş-Gaziantep province of south-central Türkiye, near the NW  
50 Syria (Melgar et al., 2023). The 2023 SE Türkiye earthquake sequence occurred in a region  
51 where a tectonically deforming complex network of faults controlled by the triple junction  
52 between the Anatolian, Arabian, and African plates (Figure. 1). The U.S. Geological Survey,  
53 National Earthquake Information Center (USGS-NEIC) located the  $M_w$  7.8 hypocenter on a  
54 splay fault south of the EAF, with a strike-slip mechanism consistent with the left-lateral  
55 motion of the East Anatolian Fault Zone (EAFZ) (Goldberg et al., 2023a, b). The main  
56 shock's epicenter and its subsequent aftershocks were consistently located along the EAF and  
57 widespread structural damage was reported in a wide region over eleven major cities and the  
58 NW Syria. The EAFZ is the major plate boundary that accommodates the westward extrusion  
59 of the Anatolia toward the Aegean Sea, and the fault zone has caused destructive earthquakes  
60 throughout recorded history (e.g., Ambraseys, 1989; Emre et al., 2018). The 2023 sequence's  
61 mainshock  $M_w$  7.8 has been the most significant and destructive earthquake along the EAFZ  
62 and surrounding fault segments since the 22 May 1971  $M_s$  6.9 Bingöl, and 24 January 2020  
63  $M_w$  6.7 Doğanyol-Sivrice earthquakes (Taymaz et al., 1991, 2021). To the south of the EAFZ,  
64 the left-lateral Dead Sea Fault (DSF) accommodates northward motion of the Arabian  
65 Peninsula relative to the African and Eurasian plates (Taymaz et al., 1991; Figure. 1).



66

67 **Figure 1.** Tectonic map of the 2023 SE Türkiye-Syria earthquake doublet and strong-motion

68 stations depicted by red-filled triangles. Two epicenters of  $M_w$  7.8 and  $M_w$  7.6 earthquakes

69 and focal mechanisms from the AFAD are shown as red stars and red beachballs, respectively.

70 Brown lines represents the fault segments used in the dynamic modeling, while black lines

71 show fault traces of mapped surface ruptures from Reitman et al. (2023). The colored-filled

72 circles show the first 11 days of relocated aftershocks (color varying according to the

73 hypocenter depth) from Melgar et al. (2023). Inset illustrates two major tectonic plates

74 (Arabian and Anatolian) and active faults (Emre et al., 2018) and plate boundaries (Bird,

75 2003), such as East Anatolian Fault Zone (EAFZ) and North Anatolian Fault Zone (NAFZ)

76 (see also Taymaz et al., 1991).

77           After the 2023 doublet sequence, many preliminary results of finite-fault source  
78 inversion based on strong ground motion, near-field geodetic data and/or teleseismic data  
79 have been published (Delouis et al., 2023; Mai et al., 2023; Melgar et al., 2023; Goldberg et  
80 al., 2023,a, b; Okuwaki et al., 2023; Xu et al., 2023). However, a highly debated controversy  
81 exists regarding the presence of a supershear rupture during the  $M_w$  7.8 event. The  
82 controversy is multifaceted. Rosakis et al. (2023) analyzed the waveforms of two near-fault  
83 stations, concluding that the supershear rupture occurred on the splay fault at a distance of  
84 about 19 km from the epicenter. Conversely, some inversion results do not support this  
85 conclusion (Delouis et al., 2023; Melgar et al., 2023). Through analyzing the rupture phase,  
86 Yao & Yang (2023) determined that the average rupture speed of the southwest section of the  
87 EAF is estimated to be  $\sim 3.1$ - $3.4$  km/s. However, this still does not eliminate the possibility of  
88 transient supershear. The preliminary dynamic rupture models also remain disputed. The first  
89 order model by Gabriel et al. (2023) is subshear, while Abdelmeguid et al. (2023) observe  
90 many transient supershear ruptures in the southwest segment and sustained supershear in the  
91 northeast segment of the EAF in their 2D simulation. Therefore, to comprehensively  
92 understand the rupture process of the 2023 Kahramanmaraş earthquake, it is necessary to  
93 conduct detailed data-constrained 3D dynamic simulations.

94           In this study, we utilize near-fault waveform data, GNSS static horizontal  
95 displacement, and surface rupture as constraints to develop a dynamic rupture model for the  
96  $M_w$  7.8 Kahramanmaraş earthquake based on cascading multi-scale network of fault system  
97 and heterogeneous initial stress. We thoroughly analyzed the triggering process of the EAF  
98 and the rupture speed of our model, followed by a discussion on the implications for the

99 seismogenic environment and widespread earthquake disaster. Finally, we discuss the  
100 earthquake physics and the future improvement for the dynamic model of this earthquake.

## 101 **2 Materials and Methods**

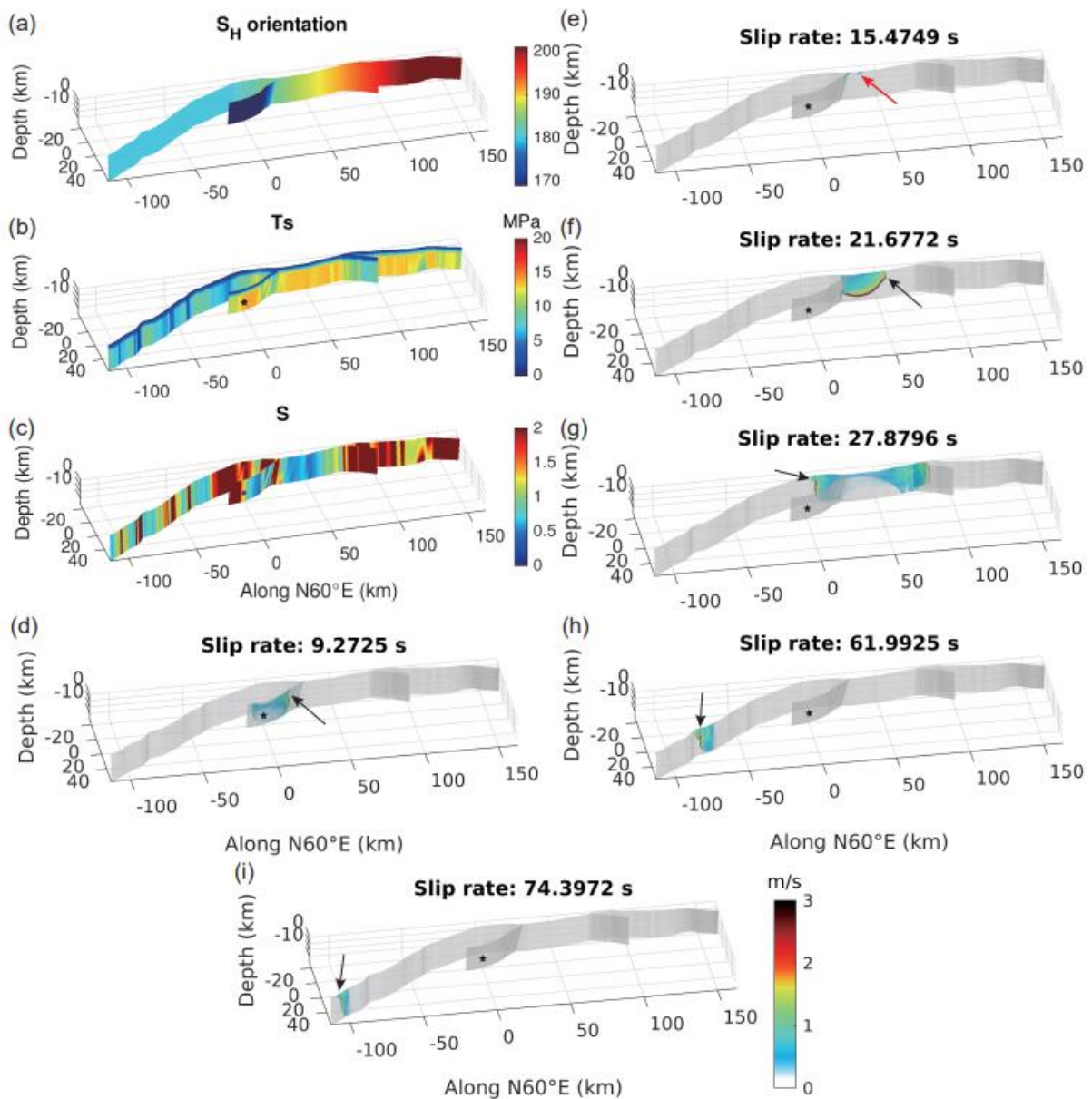
102 Fault geometry, initial stress, and rock properties control the dynamic rupture process  
103 of tectonic faults. However, these data cannot always be measured directly in-situ. In this  
104 section, we will discuss the fault model and dynamic parameters adopted based on various  
105 previous studies of the EAFZ and introduce the numerical method used for this work.

106 We construct 3D non-planar fault geometry based on the mapped surface ruptures  
107 from Reitman et al. (2023) and earthquake relocation results provided by Melgar et al. (2023).  
108 Some smaller fault branches were ignored but we kept the two major ones (Figure 1). These  
109 two branches of faults have not been mapped before. Melgar et al. (2023) designated the fault  
110 where the rupture was initiated as the Nurdağı-Pazarcık Fault (NPF). In this work, we label  
111 another branch fault as the F3 segment (Figure 1). The dip of the EAF is set to  $85^\circ$  trending  
112 southeast but bends to  $80^\circ$  trending northwest in northeastmost segment. This dip transition is  
113 the same as the fault model of Melgar et al. (2023). The dip of the NPF is set to  $80^\circ$  (trending  
114 northwest) based on the earthquake relocation results. The F3 segment shares the same dip  
115 and trend as the main portion of the EAF. All fault widths are set to 20 km.

116 The EAF is located at the intersection of the Arabian, Eurasian, and African plates,  
117 resulting in a complex stress state (Taymaz et al., 1991, 2021). Güvercin et al. (2022) studied  
118 the stress orientations based on focal mechanisms and found that the orientation varies across  
119 different fault segments. In the region that ruptured in the 2023  $M_w$  7.8 event, the direction of

120 maximum principal compressive stress  $S_H$  is roughly between N169°E and N203°E, with a  
 121 clockwise trend from southwest to northeast. Early research (Lyberis et al., 1992; Yilmaz et  
 122 al., 2006) also confirmed the same features. Therefore, after trial-and-error, the  $S_H$  orientation  
 123 is set as shown in Figure 2a.

124



125

126 **Figure 2.** Model setting and dynamic rupture results. (a) The orientation of  $S_H$ . (b) Initial

127 shear stress  $T_s$ . (c) The relative fault strength  $S$ . (d)-(i) Key snapshots of the dynamic rupture

128 process. A shared color bar is illustrated in (i). The black arrows indicate the supershear  
 129 rupture. The red arrow indicates the dynamic triggering. The black star indicates the epicenter.

130 Another factor that can constrain the initial stress is the stress shape ratio  $R$ , which is  
 131 defined as  $R = (S_v - S_H)/(S_h - S_H)$ , where  $S_h$  is the minimum principal stress,  $S_v$  is the  
 132 vertical stress. Generally, considering lithostatic pressure and pore pressure,  $S_v$  can be  
 133 described as

$$134 \quad S_v = (1 - \gamma)\rho gh. \quad (1)$$

135 Where  $\rho$  is the density of rock,  $g$  is the acceleration of gravity,  $h$  is the depth,  $\gamma$  is the pore-  
 136 fluid factor, respectively. Therefore, using a lateral pressure coefficient expressed as  $k =$   
 137  $S_H/S_v$ , we can obtain

$$138 \quad S_h = (1 - k + kR)S_v/R. \quad (2)$$

139 According to the focal mechanism inversion conducted by Yilmaz et al. (2006), the average  
 140 value of  $R$  in the Kahramanmaraş to Çelikhan segment (KC segment) of the EAF is 0.715.  
 141 This indicates that the tectonic environment in this region is characterized by transpression.  
 142 But in the southwest segment of the EAF, the tectonic environment shifts to transtension  
 143 (Lyberis et al., 1992), we assume  $R = 0.3$  in this region.

144 After trial-and-error, we set  $\gamma = 0.7$ . To prevent excessive stress drop in the deep part  
 145 and consider the increased pore pressure along depth (Rice, 1992), the stress only increases to  
 146 5 km with depth. The final initial shear stress and the relative fault strength  $S$  (defined as  
 147  $(\tau_p - \tau_0)/(\tau_0 - \tau_d)$ , where  $\tau_p$ ,  $\tau_0$  and  $\tau_d$  are the peak shear stress, the initial shear stress and  
 148 the dynamic friction stress, respectively) are shown in Figure 2b-c. We set the location of the

149 nucleation zone based on the hypoDD relocations of Melgar et al. (2023). The radius of the  
150 nucleation zone is artificially set to 1.8 km. And the shear stress of the nucleation zone is set  
151 to a value 0.1% higher than the shear strength to trigger the rupture. The distribution of  $k$  and  
152  $R$  are illustrated in Figure S1.

153 Here, slip-weakening friction law (Ida, 1972) is applied in our simulation, and also in  
154 a recent study by Taymaz et al. (2022). Khalifa et al. (2018) investigated the rock strength of  
155 the EAFZ, they found that the rock strength varied from very low to moderate from west to  
156 east in the KC segment of the fault. Thus, the friction coefficients are also heterogeneous in  
157 the fault plane (Figure S2). The critical slip distance  $D_c$  only varies with depth (Figure S3).  
158 The value of  $D_c$  is set to 0.36 m in the depth of 0-15 km and is linearly increased when the  
159 depth is larger than 15 km to mimic the brittle-ductile transition in the crust.

160 In addition, noting that our model setting is very heterogeneous, we explain the  
161 necessity of considering stress field rotation and non-uniform friction coefficients in the  
162 supplementary materials (see Text S1, Figure S5-S6). A layered seismic velocity structure  
163 (Güvercin et al., 2022) is adopted in our dynamic modeling (see Table S1). This model only  
164 provides P and S wave velocity  $V_p$  and  $V_s$ , hence we use the empirical formula (Brocher,  
165 2005) to calculate the density  $\rho$  according to  $V_p$ .

166 In this work, we use an open-source software DRDG3D, which was developed by  
167 Zhang et al. (2023) for the dynamic rupture modeling. DRDG3D is based on a nodal  
168 discontinuous Galerkin (DG) framework (Hesthaven and Warburton, 2008) with tetrahedral  
169 mesh adopted. Due to the flexibility for modeling geometric complex faults, DG methods has  
170 been widely used in dynamic rupture modeling of real or scenario earthquakes (Biemiller et

171 al., 2022; Ramos et al., 2021; Ulrich et al., 2019; Wollherr et al., 2019). DRDG3D adopts an  
172 upwind/central mixed flux scheme, which removes numerical artifacts when the near-fault  
173 asymmetric unstructured tetrahedral mesh is generated. The numerical scheme of DRDG3D  
174 reduces the dependence of mesh quality thereby increasing the efficiency. The DRDG3D has  
175 been verified by many benchmark models in the *SCEC/USGS Spontaneous Rupture Code*  
176 *Verification Project* (<https://strike.scec.org/cvws/>, Harris et al, 2009). The accuracy and  
177 efficiency of DRDG3D has been analyzed in detail by Zhang et al. (2023).

### 178 **3 Results**

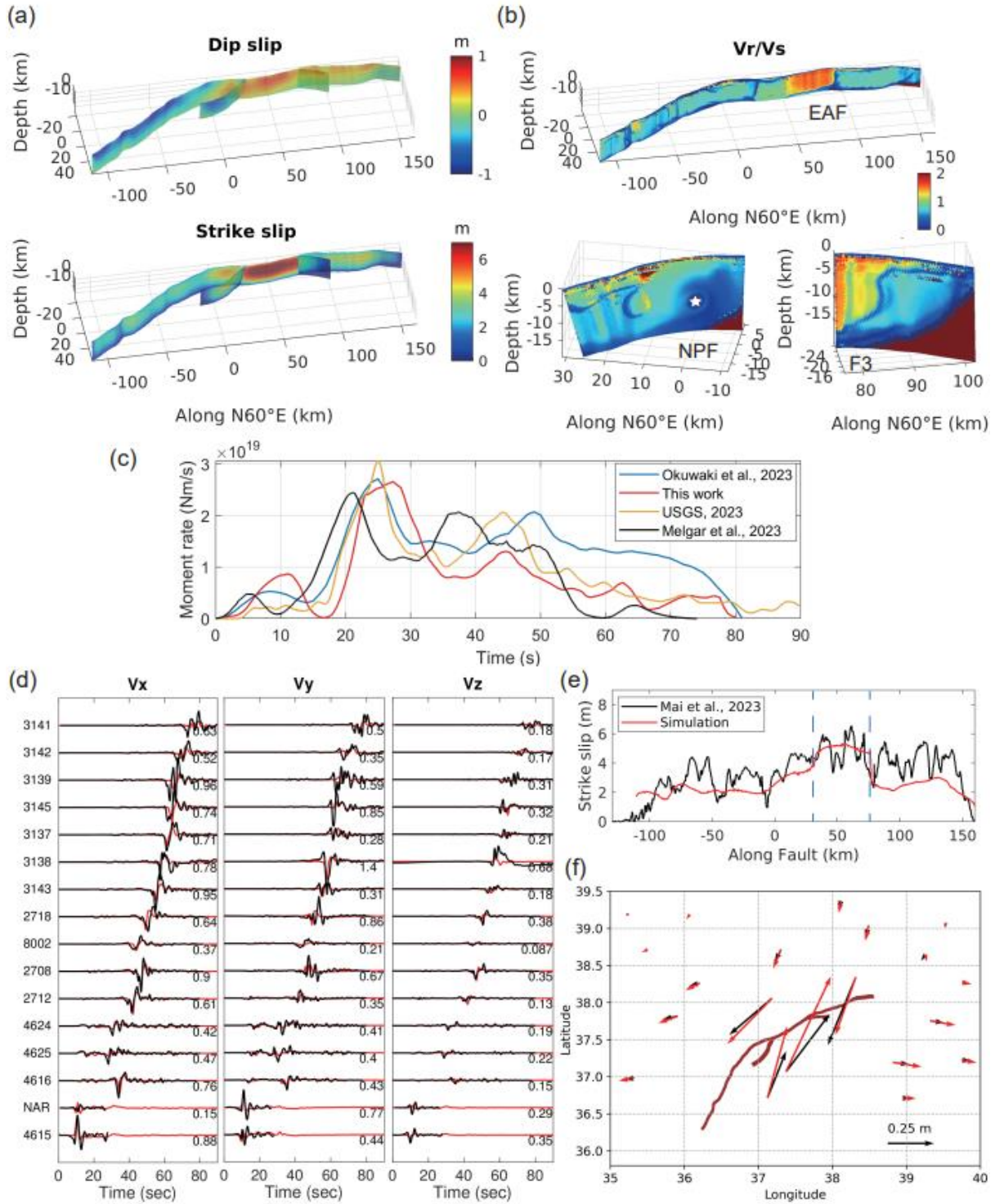
179 The fault element size of our dynamic simulation is 570 m, with the spatial-order-of-  
180 accuracy of 3. The time step is 0.0031 s and the total simulation time is 90 s. Figure 2d-i  
181 shows some key snapshots of the rupture process. The complete dynamic rupture process can  
182 be found in Movie S1. The rupture nucleated at the NPF and generated a supershear rupture  
183 at about 9 s (Figure 2d), supporting the preliminary analysis of Rosakis et al. (2023). And  
184 then, the EAF was dynamically triggered in the northeast of the junction (Figure 2e). After  
185 being triggered, the rupture propagated northeast on the EAF and transitioned to a supershear  
186 rupture very quickly (Figure 2f). As the fault strength increased along the strike, the rupture  
187 speed returned to subshear (Figure 2g). A few seconds later, the rupture began to propagate  
188 southwest. Due to the complex segmented fault geometry, the rupture speed varies frequently  
189 (see Figure 2g-i, Figure 3b). The supershear rupture encounters barriers caused by fault  
190 geometry changes, making it unsustainable. The final slip distribution of our dynamic model  
191 is presented in Figure 3a. The maximum strike-slip displacement exceeds 7 m.

192 We calculate the rupture speed by the reciprocal of the gradient of the rupture time  
193 (Figure 3b), and the rupture time definition threshold is slip rate greater than 0.001 m/s. The  
194 overall results of rupture speed are different from Melgar et al. (2023) but are similar to that  
195 of Delouis et al. (2023). There may be various reasons for the different results, such as  
196 different velocity models or data processing of different research groups. Moreover,  
197 Abdelmeguid et al. (2023) analyzed the fault normal and fault parallel components of near-  
198 fault stations. They concluded the Station NAR and 3145 showing the characteristics of  
199 supershear rupture, which also consistent with our results.

200 From the  $S$  value and the snapshot of rupture process shown in Figure 2c, we can find  
201 that the supershear rupture in the northeast section of the EAF (Figure 2f) may be caused by  
202 Burridge-Andrews mechanism, and the supershear rupture in Figure 2g should be induced by  
203 free surface. Two supershear ruptures in the southwest section of the EAF (Figure 2h-i) also  
204 started from the free surface, but the corresponding  $S$  value is also very low.

205 The rupture duration for the earthquake simulated in this study is approximately 80 s,  
206 and the moment magnitude achieved is  $M_w$  7.8665. Figure 3c compared the moment rate  
207 release process of this work, the inversion results of Melgar et al. (2023), Okuwaki et al.  
208 (2023), USGS (2023) (for details see Goldberg et al., 2023a, b). All the results show  
209 consistency in terms of duration and seismic moment release characteristics, with the  
210 maximum peak occurring at 20-30 s and the second peak at 40-50 s. These two peaks  
211 correspond to the two periods of maximum energy release for this earthquake.

212



213

214 **Figure 3.** (a) Final slip distribution of the dynamic model. (b) The ratio of rupture speed  $V_r$

215 and  $V_s$ .  $V_r/V_s$  greater than 1 indicates the supershear rupture. The three faults are drawn

216 separately and marked on the figure. There is no rupture in the crimson region except the

217 nucleation zone. The white star indicates the epicenter. (c) Moment rate release comparison.

218 (d) Comparison of waveforms of near-fault stations. The black line is the observed waveform,  
219 and the red line is the synthesized waveform, both of which are filtered to 0.01-0.4 Hz. The  
220 station name is marked on the left. The maximum absolute values of each component of the  
221 observations (m/s) are listed at the end of each seismogram (see Figure 1 for the location of  
222 the stations). (e) Comparison of surface strike-slip displacement. The red line is the  
223 simulation result, and the black line is the data provided by Mai et al. (2023). The two blue  
224 dashed lines represent the intersections of NPF (left) and F3 (right) with EAF, respectively. (f)  
225 Compared with the static horizontal displacement of GNSS. The black arrow is the observed  
226 value and the red arrow is the synthetic value.

227 Figure 3d shows a comparison of the near-fault station waveforms (filtered to 0.01-0.4  
228 Hz). Our results successfully reproduce the primary features of the observations, and the  
229 agreement in travel time between our simulation and the observations suggests that the  
230 rupture speed in our model is reasonable. Several stations at the most southwest segment of  
231 the fault are not well fitted, which may be because we ignore some small branches at the end  
232 of the fault and the 3D heterogeneous velocity models are lacking and the relatively uniform  
233 dynamic parameters. The triggering and stopping of the rupture on the small branches we  
234 ignore will produce strong ground motion, and our layered model cannot well reflect the  
235 amplification effect of the sedimentary basin. We noticed that the aforementioned stations are  
236 all located near the southwest segment of the EAF. Unfortunately, the near-fault station  
237 records in the northeast segment of the EAF were abruptly terminated for unknown reasons,  
238 which made the rupture process in the northeast segment less constrained. Nonetheless, we  
239 still select 4 stations to compare the relevant waveforms in Figure S4. The stop time of the

240 recording is very close to the arrival time of the waveforms, leading us to suspect that the  
241 cause of station damage is related to the arrival of rupture. Therefore, it is possible and  
242 acceptable that a supershear rupture occurred in the northeast segment of the EAF.

243         The detailed investigation results of surface rupture have not been seen yet, hence the  
244 surface strike-slip is compared with the on-fault displacement measured by Mai et al. (2023)  
245 based on the satellite data (Liu et al., 2022a; 2022b; Figure 3e). We have captured the first-  
246 order characteristics of surface displacement. Notably, the surface displacement on the  
247 backward side of the fault intersection has changed suddenly because of the dynamic  
248 unclamping. We also calculate the static horizontal displacement based on the triangular  
249 elastic half-space dislocation model (Nikkhoo et al., 2015; Meade, 2007) and compare to the  
250 observations (Barbot et al., 2023; Figure 3f). The observational and synthetic displacements  
251 are a general match. Some mismatches in displacement vectors may be due to the stronger  
252 spatial heterogeneity of the actual slip distribution, as well as the lack of consideration of  
253 complex medium models in the calculation of the synthesized displacement.

## 254 **4 Discussions**

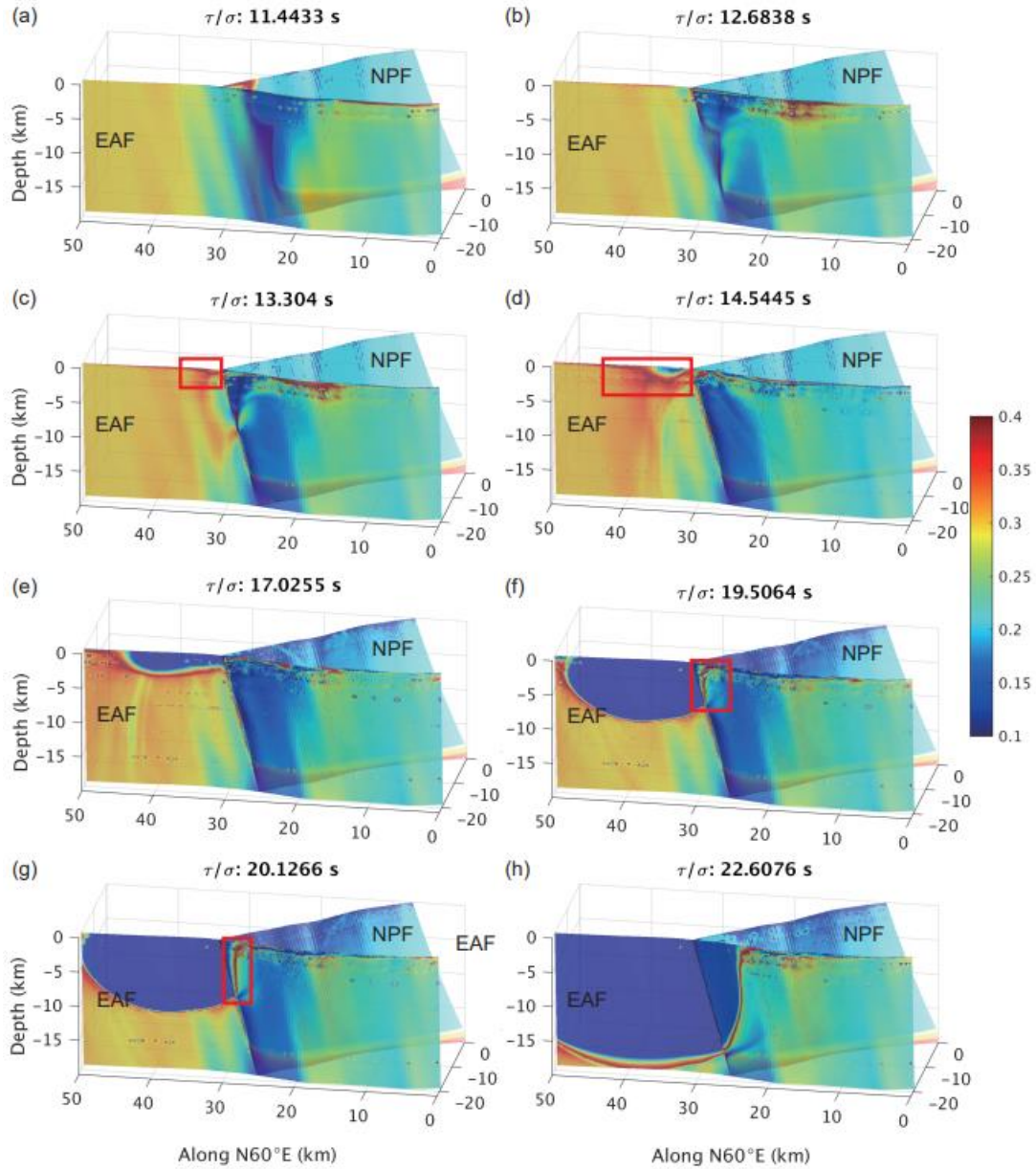
### 255 *4.1 Implications for seismogenic environment, process of EAF being triggered and* 256 *earthquake disaster*

257         Our dynamic model indicates a high initial stress level in the KC segment of the EAF.  
258 Actually, this segment has been identified as a seismic gap with Coulomb stress in an  
259 elevated state proposed by Sunbul (2019). Thus, the stress state is consistent with the current  
260 seismogenic environment. This plays a crucial role in the triggering process of the EAF.

261 Because the angle between the NSF and the EAF is about  $30^\circ$ , if the direction of  $S_H$  is close  
262 to the optimal stress orientation of one fault, it will be far from the optimal stress orientation  
263 of another fault in the range of  $N169^\circ E$ - $N203^\circ E$ . In our model, the  $S_H$  orientation of the fault  
264 junction is  $N184^\circ E$ , closer to the optimal stress orientation of the EAF. Therefore, near the  
265 fault intersection, the slip rate on the NSF decreases and the dynamic stress decreases, which  
266 is not conducive to the rupture propagates to the EAF. However, because the stress in this  
267 segment of EAF is high enough, the rupture propagated to the EAF in the northeast of the  
268 fault intersection through dynamic triggering. Figure 4 and Movie S2 show the ratio of shear  
269 stress and normal stress during the triggering process. More importantly, the high initial  
270 stress also leads to the generation of supershear rupture in the northeast segment of the EAF  
271 (Figure 3b) and accumulated enough energy to make the rupture propagates backward  
272 (Figure 4f-h).

273 The 2023  $M_w$  7.8 Kahramanmaraş earthquake reminds us of the 2001 Kokoxili  
274 earthquake in China and the 2002 Denali earthquake in USA. These two events were also  
275 nucleated on secondary faults (Antolik et al., 2004; Eberhart-Phillips et al., 2003). After the  
276 rupture propagated to the main fault, a supershear rupture occurred, and the rupture length  
277 was also greater than 300km. The difference is that these two earthquakes were unilateral  
278 rupture. In addition, the change of rupture speed will produce high-frequency seismic  
279 radiation (Vallée et al., 2008), this may also be one of the reasons for the serious damage to  
280 Hatay province in southern Türkiye. Therefore, these earthquakes serve as a reminder to  
281 remain vigilant as major faults can be triggered by earthquakes nucleated on nearby  
282 unrecognized small fault fragments, eventually evolving into giant earthquakes that cause

283 significant damage. This is especially important when there are seismic gaps along the major  
 284 fault.



285

286 **Figure 4.** The ratio of shear stress and normal stress during the triggering process. A ratio  
 287 equal to  $\mu_s$  (0.4) indicates the position of the rupture front in the EAF. (a) Before the rupture  
 288 front reaches the fault intersection. (b) The rupture front reaches the fault intersection. (c-d)  
 289 The EAF is triggered, and the red boxes indicate the trigger location. (e) The rupture  
 290 propagates northeast and the stress ratio in the backward side is very low indicating it is

291 difficult to rupture. (f-h) Enough energy is accumulated, and the rupture begins to propagate  
292 backward. The red boxes indicate that the rupture is beginning to propagate backward.

#### 293 *4.2 Open questions and future work*

294 Previous studies have suggested that the EAF is an immature fault (Galovič et al.,  
295 2020; Melgar et al., 2020; Pousse-Beltran et al., 2020; Taymaz et al., 2021). However,  
296 earthquake cycle research shows immature faults are more prone to moderate earthquakes  
297 (Thakur & Huang, 2021), this is inconsistent with the situation of the 2023 Kahramanmaraş  
298 earthquake. Therefore, does this earthquake manifest that the EAF is going to be mature? If  
299 not, why does the rupture length of an immature fault reach 300 km? Thus, there remains  
300 further research, such as radiation efficiency should be investigated in detail. Moreover, the  
301 2023 Kahramanmaraş earthquake may be another example of transient supershear ruptures on  
302 an immature strike-slip fault like the 2021 Madoi earthquake in China (Cheng et al., 2023).

303 We didn't consider the topography and the off-fault damage in the dynamic simulation,  
304 which may also affect the results. For example, terrain fluctuation is not conducive to the  
305 occurrence of free-surface-induced supershear rupture (Zhang et al., 2016). Asymmetric  
306 topography along the fault can cause normal stress perturbation of the rupture front near the  
307 free surface (Kyriakopoulos et al., 2021). Off-fault plasticity will also consume energy and  
308 influence the dynamic rupture process, necessitating a higher initial stress (Gabriel et al.,  
309 2013). Future work should also consider the rate and state friction law (Dieterich, 1994;  
310 Ruina, 1983), and discuss the impact of thermal pressurization (Rempel & Rice, 2006;  
311 Wibberley & Shimamoto, 2005) or flash heating (Goldsby & Tullis, 2011).

## 312 **5 Conclusions**

313 In this work, a data-constrained 3D dynamic rupture model with a complex fault  
314 geometry of the 2023 Kahramanmaraş  $M_w$  7.8 earthquake is established. The results show  
315 that high initial stress in the KC segment causes the EAF to be triggered. The transient  
316 supershear rupture occurs many times, and the change of fault geometry prevents the  
317 sustainability of the supershear rupture. Moreover, the triggering process of the NPF to the  
318 EAF reminds us that we should pay attention to the seismic activity of the secondary faults  
319 adjoining the major fault, and carefully study the risk of the main fault being triggered to  
320 prevent the severe casualties from repeating in the future.

## 321 **Acknowledgments**

322 The authors declare no competing interests. The authors are grateful to Editor Germán Prieto,  
323 and two anonymous reviewers for their constructive comments. We thank Dr. Jihong Liu  
324 from King Abdullah University of Science and Technology for providing the on-fault surface  
325 displacement data. The authors also thanks Dr. Suli Yao from the Chinese University of  
326 Hong Kong, Mathilde Marchandon from the Ludwig-Maximilians-Universität München, and  
327 Dr. Lingling Ye from Southern University of Science and Technology for the beneficial  
328 discussions. Tuncay Taymaz thanks to Dr. Beyza Taymaz for her phenomenal support during  
329 hectic days dealing with global media requests and organizing international scientific  
330 collaborations throughout four-weeks of sleepless nights. This work is supported by the  
331 National Natural Science Foundation of China (grant no. 42174057), Guangdong Provincial  
332 Key Laboratory of Geophysical High-resolution Imaging Technology (2022B1212010002).  
333 Tuncay Taymaz thanks to Istanbul Technical University Research Fund (ITU-BAP) and the

334 Alexander von Humboldt Foundation for providing financial support toward relevant  
335 computational resources through the Humboldt-Stiftung follow-up program. This work is  
336 supported by Center for Computational Science and Engineering at Southern University of  
337 Science and Technology.

### 338 **Open Research**

339 The dynamic rupture software DRDG3D is available at <https://github.com/wqseis/drdg3d>  
340 (last accessed February 2022). The mapped surface rupture data are from  
341 <https://doi.org/10.5066/P985I7U2> (Reitman et al. 2023). The strong ground motion data are  
342 downloaded from the Disaster and Emergency Management Authority (AFAD,  
343 <https://tadas.afad.gov.tr/event-detail/15499>). The GNSS static horizontal displacement data  
344 are available in Table S1 of Barbot et al. (2023, <https://zenodo.org/record/7879743>).

### 345 **References**

- 346 Abdelmeguid, M., Zhao, C., Yalcinkaya, E., Gazetas, G., Elbanna, A., & Rosakis, A. (2023).  
347 Revealing The dynamics of the Feb 6th 2023 M7.8 Kahramanmaraş/Pazarcik  
348 Earthquake: near-field records and dynamic rupture modeling, *EarthArXiv*,  
349 <https://doi.org/10.31223/X5066R>.
- 350 Antolik, M., Abercrombie, R. E., & Ekström, G. (2004). The 14 November 2001 Kokoxili  
351 (Kunlunshan), Tibet, earthquake: rupture transfer through a large extensional step-over,  
352 *Bulletin of the Seismological Society of America*, 94(4), 1173-1194,  
353 <https://doi.org/10.1785/012003180>.
- 354 Barbot, S., Luo, H., Wang, T., Hamiel, Y., Piatibratova, O., Javed, M. T., et al. (2023). Slip  
355 distribution of the February 6, 2023  $M_w$  7.8 and  $M_w$  7.6, Kahramanmaraş, Turkey

- 356 earthquake sequence in the East Anatolian Fault Zone, *Seismica*, 2(3),  
357 <https://doi.org/10.26443/seismica.v2i3.502>.
- 358 Biemiller, J., Gabriel, A. A., & Ulrich, T. (2022). The Dynamics of Unlikely Slip: 3D  
359 Modeling of Low - Angle Normal Fault Rupture at the Mai'iu Fault, Papua New Guinea,  
360 *Geochemistry, Geophysics, Geosystems*, 23(5), e2021GC010298,  
361 <https://doi.org/10.1029/2021gc010298>.
- 362 Bird, P. (2003). An updated digital model of plate boundaries, *Geochemistry Geophysics*  
363 *Geosystems*, 4(3), 1027, <https://doi.org/10.1029/2001GC000252>.
- 364 Brocher, T. M. (2005). Empirical Relations between Elastic Wavespeeds and Density in the  
365 Earth's Crust, *Bulletin of the Seismological Society of America*, 95(6), 2081-2092,  
366 <https://doi.org/10.1785/0120050077>.
- 367 Cheng, C., Wang, D., Yao, Q., Fang, L., Xu, S., Huang, Z., et al. (2023). The 2021 *M<sub>w</sub>* 7.3  
368 Madoi, China Earthquake: Transient Supershear Ruptures on a Presumed Immature  
369 Strike - Slip Fault, *Journal of Geophysical Research: Solid Earth*, 128(2),  
370 e2022JB024641, <https://doi.org/10.1029/2022jb024641>.
- 371 Delouis, B., van den Ende, M., & Ampuero, J.-P. (2023). Kinematic rupture model of the  
372 February 6th 2023 *M<sub>w</sub>* 7.8 Turkey earthquake from a large set of near-source strong  
373 motion records combined by GNSS offsets reveals intermittent supershear rupture,  
374 *Authorea*, <https://doi.org/10.22541/essoar.168286647.71550161/v1>.
- 375 Dieterich, J. (1994). A constitutive law for rate of earthquake production and its application  
376 to earthquake clustering, *Journal of Geophysical Research*, 99(B2), 2601-2618,  
377 <https://doi.org/10.1029/93jb02581>.

- 378 Eberhart-Phillips, D., Haeussler, P. J., Freymueller, J. T., Frankel, A. D., Rubin, C. M., Craw,  
379 P., et al. (2003). The 2002 Denali fault earthquake, Alaska: A large magnitude, slip-  
380 partitioned event, *Science*, *300*(5622), 1113-1118,  
381 <https://doi.org/10.1126/science.1082703>.
- 382 Emre, Ö., Duman, T. Y., Özalp, S., Şaroğlu, F., Olgun, Ş., Elmacı, H., & Çan T. (2018).  
383 Active fault database of Turkey, *Bulletin of Earthquake Engineering*, *16*(8), 3229–3275,  
384 <https://doi.org/10.1007/s10518-016-0041-2>.
- 385 Gabriel, A.-A., Ulrich, T., Marchandon, M., & Biemiller, J. (2023). Geodetically and  
386 seismically informed rapid 3D dynamic rupture modeling of the *M<sub>w</sub>* 7.8  
387 Kahramanmaraş earthquake, in *EGU General Assembly 2023*, edited, Vienna, Austria,  
388 <https://doi.org/10.5194/egusphere-egu23-17603>.
- 389 Gabriel, A. A., Ampuero, J. P., Dalguer, L. A., & Mai, P. M. (2013). Source properties of  
390 dynamic rupture pulses with off-fault plasticity, *Journal of Geophysical Research: Solid*  
391 *Earth*, *118*(8), 4117-4126, <https://doi.org/10.1002/jgrb.50213>.
- 392 Gallovič, F., Zahradník, J., Plicka, V., Sokos, E., Evangelidis, C., Fountoulakis, I., & Turhan,  
393 F. (2020). Complex rupture dynamics on an immature fault during the 2020 *M<sub>w</sub>* 6.8  
394 Elazığ earthquake, Turkey, *Communications Earth & Environment*, *1*(1),  
395 <https://doi.org/10.1038/s43247-020-00038-x>.
- 396 Goldberg, D. E., Taymaz, T., Reitman, N. G., Hatem, A. E., Yolsal-Çevikbilen, S., Barnhart,  
397 W. D., et al. (2023a). Rapid Characterization of the February 2023 Kahramanmaraş,  
398 Türkiye, Earthquake Sequence, *The Seismic Record*. *3*(2), 156–167,  
399 <https://doi.org/10.1785/0320230009>.

- 400 Goldberg, D. E., Taymaz, T., Yeck, W. L., Barnhart, W. D., Yolsal-Çevikbilen, S., Irmak, T.  
401 S., et al. (2023b). Supporting data and models for characterizing the February 2023  
402 Kahramanmaraş, Türkiye, earthquake sequence, U.S. Geol. Surv. Data Release,  
403 <https://doi.org/10.5066/P9R6DSVZ>.
- 404 Goldsby, D. L., & Tullis, T. E. (2011). Flash Heating leads to low frictional strength of  
405 crustal rocks at earthquake slip rates, *Science*, 6053(14), 216-218,  
406 <https://doi.org/10.1126/science.1207902>.
- 407 Güvercin, S. E., Karabulut, H., Konca, A. Ö., Doğan, U., & Ergintav, S. (2022). Active  
408 seismotectonics of the East Anatolian Fault, *Geophysical Journal International*, 230(1),  
409 50-69, <https://doi.org/10.1093/gji/ggac045>.
- 410 Harris, R. A., Barall, M., Archuleta, R., Dunham, E., Aagaard, B., Ampuero, J. P., et al.  
411 (2009). The SCEC/USGS dynamic earthquake rupture code verification exercise,  
412 *Seismological Research Letters*, 80(1), 119–126, <https://doi.org/10.1785/gssrl.80.1.119>.
- 413 Hesthaven, J.S. & Warburton, T., (2008). *Nodal Discontinuous Galerkin Methods:*  
414 *Algorithms, Analysis, and Applications*, (vol. 54). Springer New York.  
415 <https://doi.org/10.1007/978-0-387-72067-8>.
- 416 Ida, Y. (1972). Cohesive force across the tip of a longitudinal-shear crack and Griffith's  
417 specific surface energy, *Journal of Geophysical Research*, 77(20), 3796-3805,  
418 <https://doi.org/10.1029/JB077i020p03796>.
- 419 Khalifa, A., Çakır, Z., Owen, L., & Kaya, Ş. (2018). Morphotectonic analysis of the East  
420 Anatolian Fault, Turkey, *Turkish Journal of Earth Sciences*, 27(2), 110-126,  
421 <https://doi.org/10.3906/yer-1707-16>.

- 422 Kyriakopoulos, C., Wu, B., and Oglesby D. D. (2021), Asymmetric topography causes  
423 normal stress perturbations at the rupture front: The case of the Cajon pass, *Geophysical*  
424 *Research Letters*, 48(20), e2021GL095397, <https://doi.org/10.1029/2021GL095397>.
- 425 Liu, J., Hu, J., Li, Z., Ma, Z., Shi, J., Xu, W., & Sun, Q. (2022a). Three-Dimensional Surface  
426 Displacements of the 8 January 2022 Mw6.7 Menyuan Earthquake, China from  
427 Sentinel-1 and ALOS-2 SAR Observations. *Remote Sensing*, 14(6), 1404,  
428 <https://doi.org/10.3390/rs14061404>.
- 429 Liu, J., Hu, J., Li, Z. Ma, Z., Wu, L., Jiang, W., Feng, G., & Zhu, J. (2022b). Complete three-  
430 dimensional coseismic displacements due to the 2021 Maduo earthquake in Qinghai  
431 Province, China from Sentinel-1 and ALOS-2 SAR images. *Science China Earth*  
432 *Science*, 65(4), 687–697, <https://doi.org/10.1007/s11430-021-9868-9>.
- 433 Lyberis, N., Yurur, T., Chorowicz, J., Kasapoglu, E., & Gundogdu, N. (1992). The East  
434 Anatolian Fault: an oblique collisional belt, *Tectonophysics*, 204(1-2), 1-15,  
435 [https://doi.org/10.1016/0040-1951\(92\)90265-8](https://doi.org/10.1016/0040-1951(92)90265-8).
- 436 Mai, P. M., Aspiotis, T., Aquib, T. A., Cano, E. V., Castro-Cruz, D., Espindola-Carmona, A.,  
437 et al. (2023). The Destructive Earthquake Doublet of 6 February 2023 in South-Central  
438 Türkiye and Northwestern Syria: Initial Observations and Analyses, *The Seismic Record*,  
439 3(2), 105-115, <https://doi.org/10.1785/0320230007>.
- 440 Meade, B. J. (2007). Algorithms for the calculation of exact displacements, strains, and  
441 stresses for triangular dislocation elements in a uniform elastic half space. *Computers &*  
442 *geosciences*, 33(8), 1064-1075, <https://doi.org/10.1016/j.cageo.2006.12.003>.

- 443 Melgar, D., Ganas, A., Taymaz, T., Valkaniotis, S., Crowell, B. W., Kapetanidis, V., et al.,  
444 (2020). Rupture kinematics of 2020 January 24 Mw 6.7 Doğanyol-Sivrice, Turkey  
445 earthquake on the East Anatolian Fault Zone imaged by space geodesy, *Geophysical*  
446 *Journal International*, 223(2), 862–874, <https://doi.org/10.1093/gji/ggaa345>.
- 447 Melgar, D., Taymaz, T., Ganas, A., Crowell, B., Öcalan, T., Kahraman, M., et al. (2023).  
448 Sub- and super-shear ruptures during the 2023  $M_w$  7.8 and  $M_w$  7.6 earthquake doublet  
449 in SE Türkiye, *Seismica*, 2(3), 1-10, <https://doi.org/10.26443/seismica.v2i3.387>.
- 450 Nikkhoo, M., & Walter, T. R. (2015). Triangular dislocation: an analytical, artefact-free  
451 solution. *Geophysical Journal International*, 201(2), 1119-1141,  
452 <https://doi.org/10.1093/gji/ggv035>.
- 453 Okuwaki, R., Yagi, Y., Taymaz, T., & Hicks, S. P. (2023). Multi-scale rupture growth with  
454 alternating directions in a complex fault network during the 2023 south-eastern Türkiye  
455 and Syria earthquake doublet, *Geophysical Research Letters*, 50(12), e2023GL103480.  
456 <https://doi.org/10.1029/2023GL103480>.
- 457 Pousse - Beltran, L., Nissen, E., Bergman, E. A., Cambaz, M. D., Gaudreau, É., Karasözen,  
458 E., & Tan, F. (2020). The 2020  $M_w$  6.8 Elazığ (Turkey) Earthquake Reveals Rupture  
459 Behavior of the East Anatolian Fault, *Geophysical Research Letters*, 47(13),  
460 e2020GL088136, <https://doi.org/10.1029/2020gl088136>.
- 461 Ramos, M. D., Huang, Y., Ulrich, T., Li, D., Gabriel, A. A., & Thomas, A. M. (2021).  
462 Assessing Margin-Wide Rupture Behaviors Along the Cascadia Megathrust With 3-D  
463 Dynamic Rupture Simulations, *Journal of Geophysical Research: Solid Earth*, 126(7),  
464 e2021JB022005, <https://doi.org/10.1029/2021JB022005>.

- 465 Reitman, N.G., Briggs, R.W, Barnhart, W.D., Thompson, J.A., DuRoss, C.B., Hatem, A.E.,  
466 Gold, R.D., Mejstrik, J.D. (2023). Preliminary fault rupture mapping of the 2023 M7.8  
467 and M7.5 Türkiye Earthquakes. <https://doi.org/10.5066/P985I7U2>, last accessed March  
468 2023.
- 469 Rempel, A. W., & Rice, J. R. (2006). Thermal pressurization and onset of melting in fault  
470 zones, *Journal of Geophysical Research*, 111(B9),  
471 <https://doi.org/10.1029/2006jb004314>.
- 472 Rice, J. R. (1992). *Fault Stress States, Pore Pressure Distributions, and the Weakness of the*  
473 *San Andreas Fault* (Vol. 51, pp. 475–503). Academic Press Ltd.  
474 [https://doi.org/10.1016/s0074-6142\(08\)62835-1](https://doi.org/10.1016/s0074-6142(08)62835-1).
- 475 Rosakis, A., Abdelmeguid, M., & Elbanna, A. (2023). Evidence of Early Supershear  
476 Transition in the Feb 6th 2023 *M<sub>w</sub>* 7.8 Kahramanmaraş Turkey Earthquake From Near-  
477 Field Records, *EarthArXiv*, <https://doi.org/10.31223/X5W95G>.
- 478 Ruina, A. (1983). Slip instability and state variable friction laws, *Journal of Geophysical*  
479 *Research*, 88(B12), 10359-10370, <https://doi.org/10.1029/JB088iB12p10359>.
- 480 Sunbul, F. (2019). Time-dependent stress increase along the major faults in eastern Turkey,  
481 *Journal of Geodynamics*, 126, 23-31, <https://doi.org/10.1016/j.jog.2019.03.001>.
- 482 Taymaz, T., Eyidoğan, H., & Jackson J. A. (1991). Source parameters of large earthquakes in  
483 the East Anatolian Fault Zone (Turkey), *Geophysical Journal International*, 106(3),  
484 537–550, <https://doi.org/10.1111/j.1365-246X.1991.tb06328.x>.
- 485 Taymaz, T., Ganas, A., Yolsal-Çevikbilen, S., Vera, F., Eken, T., Erman, C., et al. (2021).  
486 Source mechanism and rupture process of the 24 January 2020 *M<sub>w</sub>* 6.7 Doğanyol-

- 487 Sivrice earthquake obtained from seismo- logical waveform analysis and space geodetic  
488 observations on the East Anatolian Fault Zone (Turkey), *Tectonophysics*, 804, 228745,  
489 <https://doi.org/10.1016/j.tecto.2021.228745>.
- 490 Taymaz, T., Yolsal-Çevikbilen, S., Irmak, T.S., Vera, F., Liu, C., Eken, T., et al. (2022).  
491 Kinematics of the 30 October 2020 Mw 7.0 Néon Karlovásion (Samos) Earthquake in  
492 the Eastern Aegean Sea: Implications on Source Characteristics and Dynamic Rupture  
493 Simulations, *Tectonophysics*, 826, 229223, <https://doi.org/10.1016/j.tecto.2022.229223>.
- 494 Thakur, P., & Huang, Y. (2021). Influence of Fault Zone Maturity on Fully Dynamic  
495 Earthquake Cycles, *Geophysical Research Letters*, 48(17),  
496 <https://doi.org/10.1029/2021gl094679>.
- 497 Ulrich, T., Gabriel, A.-A., Ampuero, J.-P., & Xu, W. (2019). Dynamic viability of the 2016  
498 Mw 7.8 Kaikoura earthquake cascade on weak crustal faults, *Nature Communications*,  
499 10(1), 1213, <https://doi.org/10.1038/s41467-019-09125-w>.
- 500 U.S. Geological Survey (2023). Event page for the M 7.8 - Central Turkey, earthquake,  
501 <https://earthquake.usgs.gov/earthquakes/eventpage/us6000jllz/>, last accessed March  
502 2023.
- 503 Vallée, M., Landès, M., Shapiro, N. M., & Klinger, Y. (2008). The 14 November 2001  
504 Kokoxili (Tibet) earthquake: High-frequency seismic radiation originating from the  
505 transitions between sub-Rayleigh and supershear rupture velocity regimes, *Journal of*  
506 *Geophysical Research*, 113(B7), B07305, <https://doi.org/10.1029/2007jb005520>.

- 507 Wibberley, C. A. J., & Shimamoto, T. (2005). Earthquake slip weakening and asperities  
508 explained by thermal pressurization, *Nature*, 436(7051), 689-692,  
509 <https://doi.org/10.1038/nature03901>.
- 510 Wollherr, S., Gabriel, A. A., & Mai, P. M. (2019). Landers 1992 “Reloaded”: Integrative  
511 Dynamic Earthquake Rupture Modeling, *Journal of Geophysical Research: Solid Earth*,  
512 124(7), 6666-6702, <https://doi.org/10.1029/2018jb016355>.
- 513 Xu, L., Mohanna, S., Meng, L., Ji, C., Ampuero, J.-P., Yunjun, Z., et al. (2023). The 2023  
514 *M<sub>w</sub>* 7.8 Kahramanmaraş, Turkey earthquake: a multi-segment rupture in a millennium  
515 supercycle, *Research Square*, <https://doi.org/10.21203/rs.3.rs-2747911/v1>.
- 516 Yao, S., & Yang, H. (2023). Rupture phase in near-fault records of the 2023 Turkey *M<sub>w</sub>* 7.8  
517 earthquake, *EarthArXiv*, <https://doi.org/10.31223/X51662>.
- 518 Yilmaz, H., Over, S., & Ozden, S. (2006). Kinematics of the East Anatolian Fault Zone  
519 between Türkoğlu (Kahramanmaraş) and Çelikhan (Adiyaman), eastern Turkey, *Earth*  
520 *Planets Space*, 58(11), 1463-1473, <https://doi.org/10.1186/BF03352645>.
- 521 Zhang, W., Liu, Y., & Chen, X. (2023). A Mixed-Flux-Based Nodal Discontinuous Galerkin  
522 Method for 3D Dynamic Rupture Modeling, *Journal of Geophysical Research: Solid*  
523 *Earth* 128(6), e2022JB025817. <https://doi.org/10.1029/2022JB025817>.
- 524 Zhang, Z., Xu, J., & Chen, X. (2016). The supershear effect of topography on rupture  
525 dynamics, *Geophysical Research Letters*, 43(4), 1457-1463,  
526 <https://doi.org/10.1002/2015gl067112>.